Available online at www.sciencedirect.com

ScienceDirect

journal homepage: www.elsevier.com/locate/he

# Controlling the compactness and $sp^2$ clusters to reduce interfacial damage of amorphous carbon/316L bipolar plates in PEMFCs

*Hao Li* [a,b], *Yang Xin* [a], *Keiji Komatsu* [c], *Peng Guo* [a,**], *Guanshui Ma* [a], *Peiling Ke* [a,b], *Kwang-Ryeol Lee* [a,d], *Hidetoshi Saito* [a,c], *Aiying Wang* [a,b,*]

[a] *Key Laboratory of Marine Materials and Related Technologies, Zhejiang Key Laboratory of Marine Materials and Protective Technologies, Ningbo Institute of Materials Technology and Engineering, Chinese Academy of Sciences, 315201, Ningbo, PR China*

[b] *Center of Materials Science and Optoelectronics Engineering, University of Chinese Academy of Sciences, 100049, Beijing, PR China*

[c] *Graduate School of Engineering, Nagaoka University of Technology, 940-2188, Nagaoka, Japan*

[d] *Computational Science Center, Korea Institute of Science and Technology, Seoul, 136-791, Republic of Korea*

## HIGHLIGHTS

- Quantitative analysis of the plasma state by the single Langmuir probe.
- Compactness of a-C films by testing their density with X-ray reflectivity method.
- Reveal plasma states and film compactness on corrosion resistance and conductivity.

## GRAPHICAL ABSTRACT

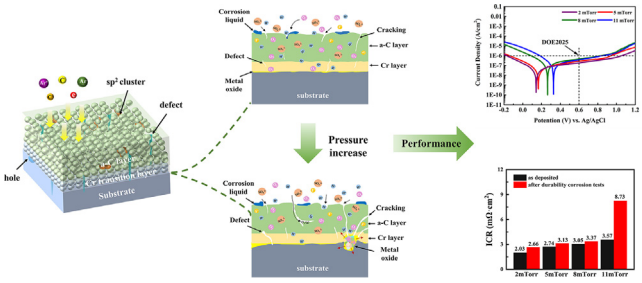


## ARTICLE INFO

*Article history:*
Received 1 November 2021
Received in revised form
20 January 2022
Accepted 22 January 2022
Available online 15 February 2022

*Keywords:*
PEMFC
Amorphous carbon film

## ABSTRACT

In proton exchange-membrane fuel cells, the compactness and composition of amorphous carbon (a-C) films directly affect the interface-induced degradation of a-C-coated metallic bipolar plates, but their roles and synergistic effects are ambiguous. In this study, by changing the working pressure, the compactness and composition of a-C are adjusted, and the relationship among the plasma state, microstructure, and performance of coated 316L stainless steel are studied. Results show that, at 2 mTorr, a high ionization degree of the plasma causes high compactness (highest density 2.52 g/cm$^3$) and large $sp^2$ cluster size in a-C films, resulting in their best performance. At 11 mTorr, the low ionization degree causes their loose structure and large $sp^2$ cluster size. The possible galvanic coupling effect can result in serious interface damage and the highest Fe ions concentration of 13.05 ppm

* *Corresponding author*. Center of Materials Science and Optoelectronics Engineering, University of Chinese Academy of Sciences, 100049, Beijing, PR China.
** *Corresponding author*.
E-mail addresses: guopeng@nimte.ac.cn (P. Guo), aywang@nimte.ac.cn (A. Wang).

https://doi.org/10.1016/j.ijhydene.2022.01.173

Bipolar plates
Compactness and composition
Plasma states

after a potentiostatic test. Thus, high compactness and large $sp^2$ cluster sizes should be obtained simultaneously to improve their performance.



## Introduction

To solve the global problems created by the energy crisis and environmental pollution, various forms of fuel cells have been under development for decades. For example, proton exchange-membrane fuel cells (PEMFCs) have been widely used in transportation, aviation, etc., owing to their advantages of low operating temperature, zero emission, and high energy conversion rate [1,2]. As a core multifunctional component, bipolar plates (BPPs) should provide high electrical and thermal conductivity, low interfacial contact resistance (ICR), and good corrosion resistance in an acidic and humid working environment, BPPs performance can directly affect the service life and commercialization process of PEMFCs.

Metallic BPPs are promising candidates as substitutes for traditional graphite plates due to their easy machinability, low cost, and good mechanical properties[3-5]. Nevertheless, under the harsh acid conditions of PEMFCs, metallic BPPs suffer from severe corrosion. The subsequent dissolution of metal ions and formation of a passive layer would result in deteriorated performance and reduced service life of PEMFCs [3–5].

Surface coating technology can not only maintain the excellent mechanical properties and good machining properties of metal plates, but also improve their electrical conductivity and corrosion resistance, thus ensuring the long-term effective operation of PEMFCs. Among the possible options, noble metal films have excellent corrosion resistance and electrical conductivity, but their high cost is not conducive to large-scale commercial production [6–8]. Metal nitride films have low cost and high electrical conductivity, but they are prone to local corrosion, which limits their application in the corrosion resistance of metal plates [9–12]. Although some metal oxide films, such as IrO2, and SnO2 could ensure both high conductivity and corrosion resistance in harsh acidic environment, the key barrier for their application were the poor adhesion and weak stability [13–15]. Owing to their excellent conductivity, corrosion resistance, and low cost for large-scale production, amorphous carbon (a-C) films have attracted extensive attention and have shown tremendous potential for the protection of metallic BPPs [16]. However, in practical applications, the degradation of a-C/metallic BPPs still exists during long-term operation [17], due to the unavoidable interface damage and increased interfacial contact resistance (ICR) [18–20].

Many researchers have tried to retard the interface damage by changing the $sp^2/sp^3$ ratio and the compactness of the a-C films [21,22]. For example, Wu et al. [23] fabricated a series of a-C films with different *trans*-layer by direct current magnetron sputtering (DCMS) and claimed that the interlocking structure between the Cr intermediate layer and the a-C film prevented the corrosive liquid from reaching the 304 stainless steel, which greatly improved the performance of the substrate. Wu et al. [24] found that a higher $sp^2/sp^3$ ratio in a-C can cause a lower ICR. From the point of compactness, Bi et al. [25] confirmed that the corrosion resistance had a very strong correlation with the compactness and composition of a-C films fabricated by DCMS. Yi et al. [26] conducted 24 h electrochemical corrosion durability tests and found that the a-C films with compact structure and high $sp^2$ content could greatly optimize the performance of stainless steel bipolar plates. Our previous work also affirmed that the residual chromium oxides at the a-C/316L stainless steel interface resulted in increased ICR values [27], and the interlocking interface structure can hinder the interface damage [28,29]. Specifically, both $sp^2/sp^3$ and the compactness affect the performance of a-C/metallic BPPs, but the role of each factor and their synergistic effects are ambiguous. In particular, the compactness of a-C films is usually determined from their morphology in this field, and qualitative or quantitative analyses are necessary. In addition, the two parameters mainly depend on the characteristics of the plasma during the deposition processes.

However, research on the influence of the plasma state is limited in this area, which hinders the optimization of a-C/metallic BPPs in PEMFCs. In DCMS, the working pressure is easy to adjust and can significantly change the incident ion flux and ion energy, which will directly affect the growth process and the microstructure of a-C films [30–32]. Therefore, in this work, a series of a-C films were deposited on 316L stainless steel (316LSS) substrates using DCMS, and the $sp^2/sp^3$ ratio and compactness were adjusted by changing the working pressure. Plasma states were analyzed using a single Langmuir probe. The compactness of the a-C films was estimated according to the $sp^2/sp^3$ ratio and density, which were characterized by XPS and the X-ray reflectivity (XRR) method, respectively. Their corrosion resistance was evaluated by typical electrochemical corrosion tests, according to the U.S. Department of Energy (DOE 2025) standard [33]. The ICR was also measured before and after the electrochemical corrosion tests. The effects of the compactness and composition of the a-C films on their corrosion resistance and conductivity were discussed, which could provide new insights into the design of high-performance a-C films for metallic BPPs in PEMFCs.

## Experimental section

### *Sample preparation*

316LSS (Φ1.5 mm × 3 mm) plates and p-type Si (100) wafers were used as substrates. All a-C films were deposited by the

DCMS technique using a graphite (380 mm × 100 mm × 7 mm, 99.99 wt%) target and a chromium (380 mm × 100 mm × 7 mm, 99.999 wt%) target, as shown in Fig. 1. Prior to deposition, the substrates were cleaned with acetone and alcohol in an ultrasonic cleaner for 30 min. Subsequently, the substrates were installed on a substrate holder in the chamber. When the base pressure in the vacuum chamber was below $3 \times 10^{-2}$ mTorr, Ar gas was introduced, and the targets were cleaned by magnetron sputtering with the shutters closed for 10 min. The substrates were then etched with Ar plasma by the linear ion source under a DC pulsed substrate bias of −50 V for 30 min to remove the surface oxide layer. To increase the film-substrate adhesion strength, a chromium interlayer with a thickness of 95 ± 10 nm was deposited by high-power impulse magnetron sputtering with a pulse width and frequency of 100 μs and 500 Hz, respectively [34]. Then, a 200 nm a-C layer was deposited by DCMS with a bias of −200 V, a sputtering power of 1.2 kW. The working pressure (2, 5, 8, and 11 mTorr) was varied to adjust the plasma state and the microstructure of the a-C films. Additional experimental details can be found in our previous publications [35,36].

### *Plasma diagnostic technology*

The effect of working pressure on the growth of a-C films was investigated through plasma diagnosis using the single Langmuir probe system (LP-500 ALP system, Impedans Ltd.). The single Langmuir probe was made of tungsten wire and had a radius of 0.35 mm. The length of the tip exposed in the plasma was 8.5 mm. The unexposed part of the tungsten wire was encapsulated in a ceramic tube. The distance between the probe tip and the target surface was 10 cm. The time-integral mode was applied during the tests. A variable voltage was supplied to this probe in the range −12 V to +2 V, and the current-voltage (I–V) characteristics were measured. In this study, the electron density was used to determine the plasma conditions by the variations in the working pressure. In quasi-neutral non-equilibrium plasma, the electron density $n_e$ can be determined from the following equation:

$$n_e = \frac{1}{0.6es}\sqrt{\frac{M_i}{kT_e}} \cdot I_{is} \quad (1)$$

where $e$ is the charge of the electron, $s$ is the area of the exposed probe surface, $M_i$ is the ion mass of the gaseous ion, $k$ is Boltzmann's constant, and $I_{is}$ is the ion saturation current. The plasma potential was also measured to estimate the change in the incident ion energy, probably with the combination of substrate bias.

### *Microstructural characterizations*

XRR analysis was employed to investigate the density of the a-C films using an X-ray diffractometer (SmartLab, Rigaku). The Cu kα radiation source and the wavelength of 1.54 Å were selected for the tests, and the incident angle was adjusted in the range of 0.03–1.63° and measured with a step of 0.004°. The thickness and density of the films were analyzed using the GlobalFit software, and a theoretical model was generated to fit the experimental data [37].

The thickness, surface, and cross-sectional morphology of the a-C films were studied by a scanning electron microscope (SEM, Verios G4 UC, US) and a scanning probe microscope

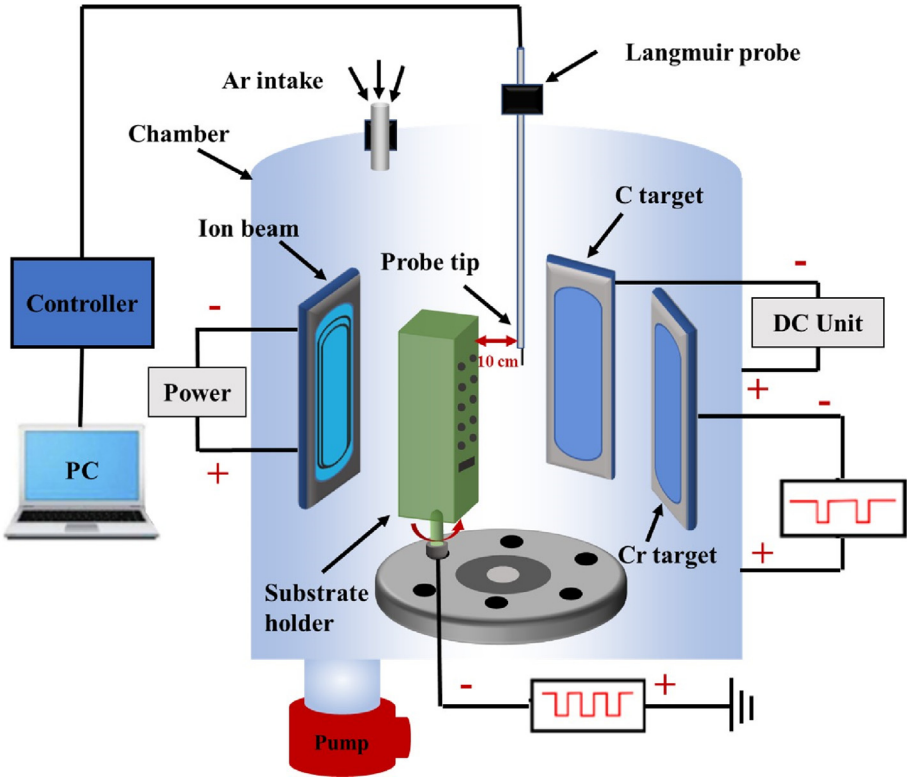


**Fig. 1 – The schematic graph of the DCMS equipment and the single Langmuir probe system.**

(SPM, Dimension 3100, US). X-ray photoelectron spectroscopy (XPS, Axis ultradld, Japan) was used to evaluate the composition and atom binding state in the a-C films. A confocal micro-Raman spectrometer (Renishaw inVia Reflex, UK, 532 nm) was used to analyze the carbon bond structure [38]. A transmission electron microscope (TEM, Tecnai F20, US) was used to obtain the morphology. Selected area electron diffraction (SAED) and the electron energy loss spectrum (EELS) were also used to obtain the microstructure and $sp^2$ fraction of the a-C films.

### *Electrochemical behaviors and ICR*

To analyze the corrosion resistance of the modified 316LSS, electrochemical corrosion tests were carried out using the Gamry electrochemical workstation (Reference 600$^+$, US). Corrosion behavior was measured using a traditional three-electrode system. The Ag/AgCl electrode was used as the reference electrode, the sample acted as the working electrode, and the platinum plate was used as the counter electrode. During electrochemical corrosion tests, samples were conducted under simulated operating conditions of PEMFCs (0.5 M $H_2SO_4$ + 5 ppm HF, 80 °C). Before the electrochemical corrosion tests, the open circuit potential (OCP) continued to run for 1 h to ensure the electrochemical stability of the system [16,39,40]. Then the potentiodynamic polarization was measured from −0.2 V vs. Ag/AgCl ranging to +1.2 V vs. Ag/AgCl at a scanning rate of 0.5 mV/s. Following that, the potentiostatic test was carried out at 0.6 V vs. Ag/AgCl for 12 h to investigate the corrosion resistance and service life of the modified 316LSS plates in the simulated PEMFC cathode operating environment. Additionally, after the 12 h potentiostatic test, the corrosion solution was collected, and the concentrations of Fe and Cr ions were detected by an inductively coupled plasma emission spectrometer (ICP-OES, Spectro Arcos II, Germany) [41,42].

To assess the ICR, voltammetry was performed to acquire the electrical resistivity between the coated samples and gold-coated copper plates [2,43,44]. All the test samples were sandwiched between two carbon papers (Toray TGP-H-060) with an applied pressure of 1.38 MPa (DOE2025) and 1.5 MPa (DOE2020), respectively. The ICR values were calculated according to the DOE standard.

## Results and discussion

### *Film growth and density*

In this study, the plasma density and plasma potential during the deposition of a-C films were measured. Fig. 2a shows the typical I–V curve measured by the single Langmuir probe with the variation of working pressure. Generally, the I–V characteristics can be divided into three regions: (1) ion-current saturation region ($I_{is}$), (2) transition region, and (3) electron-current saturation region ($I_{es}$). The $I_{is}$ region showed that the probe current was mainly due to the positive ion being attracted to the probe. The transition region showed that there was electron diffusion to the probe. The current varied exponentially with the probe voltage until the voltage was equal to the plasma potential ($V_p$). The $I_{es}$ region occurred when the probe current was mainly due to the electrons being attracted to the probe, which implies that we only need to analyze the electron density and plasma potential. Thus, the transition region and the ion-current saturation region need to be considered, as shown in Fig. 2a. With the same probe voltage, the probe current increased with the variation in working pressure from 2 mTorr to 8 mTorr increase in electron density. The I–V curve at 11 mTorr coincided with the curve at 8 mTorr, which means that a further increase in the working pressure did not lead to a higher electron density.

In Fig. 2b, from 2 mTorr to 8 mTorr, both the electron density and plasma potential showed continuous upward trends. The kinetic energy of individual incident ions would have a small increase due to the increase in plasma potential from approximately 3 V–5 V, since the working pressure increased four times, while the corresponding electron density only increased by 33%. This means that the ionization degree of the DCMS plasma decreased sharply with an increase in the working pressure. In general, the improved Ar atom density leads to an increase in the electron collision probability, and the electron temperature is

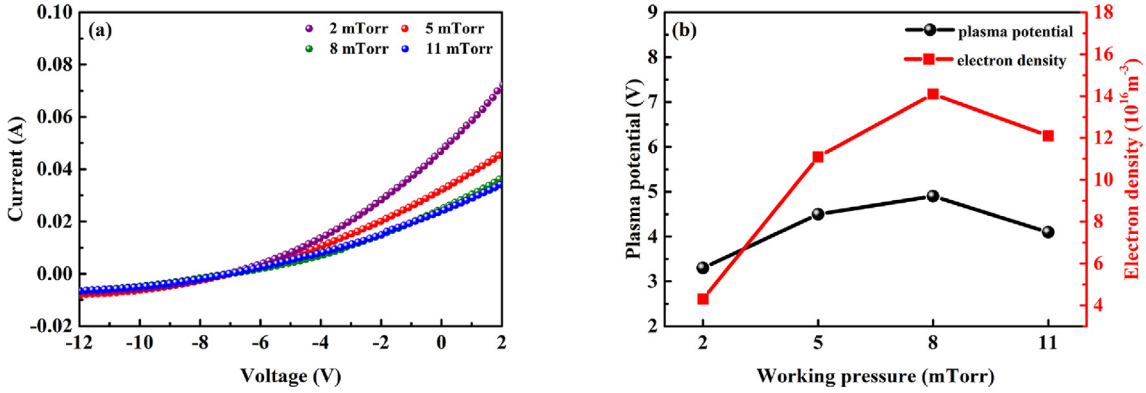


**Fig. 2 – (a) Typical I–V curve at different working pressure conditions; (b) the electron density and the plasma potential during the deposition process of a-C films at different working pressures.**

reduced in the constant discharge power mode; that is, the ratio of carbon atoms in the plasma increases. When the working pressure was increased to 11 mTorr, both the electron density and plasma potential decreased, suggesting a lower ionization degree and kinetic energy of individual incident ions.

XRR is a non-destructive technique for characterizing film thickness, surface roughness, and density with high resolution [45,46]. In Fig. 3, the experimental data of the a-C films at different working pressures matched each simulated section well. Moreover, the fringe period can could be observed in every fitting curve, which indicates indicated the single-layer structure of the a-C films. By fitting the critical angle ($\theta_c$) in the curve, the average density ($\rho$) can be calculated according to the following formula [47–49].

$$\rho = \left[\frac{\pi\theta_c^2}{N_A r_e \lambda^2}\right]\left[\frac{M_C}{Z_C}\right] \quad (2)$$

where $\theta_c$ is the critical angle in radians, $r_e$ is the electron radius, $N_A$ is Avogadro's number, $\lambda$ is the wavelength used by the instrument, $Z_C$ is the atomic number of the C atom, and $M_C$ is the molar mass of the C atom. The $\rho$ values of the as-deposited a-C films at 2, 5, 8, and 11 mTorr were 2.52, 2.01, 2.04 and 2.18 g/cm$^3$, respectively.

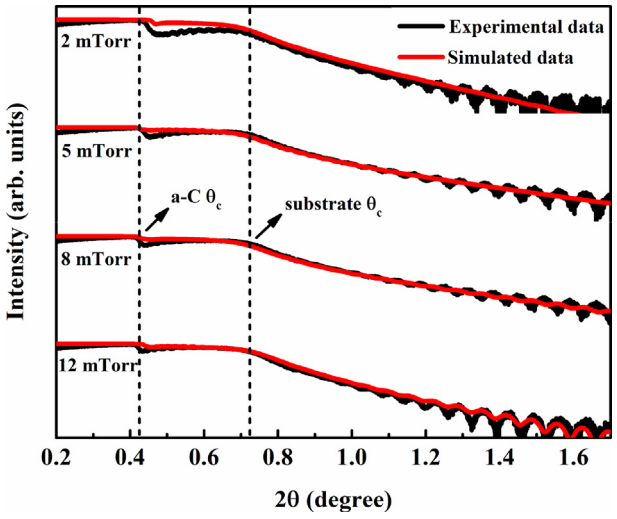


**Fig. 3 – The measured and simulated X-ray reflectivity data for a-C films deposited at various working pressures.**

### *Microstructural characterization*

The Raman spectra were divided into two peaks by Gaussian functions to ensure that the center of the D peak was around 1350 cm$^{-1}$, and that of the G peak was around 1560 cm$^{-1}$ [38,50], as shown in Fig. S2a the Supporting Information. In general, the D and G peaks represent the breathing mode of the carbon atoms in the ring and the tensile vibration of the carbon atoms in both the ring and carbon chains, respectively [51–54]. The sp$^2$/sp$^3$ ratio, sp$^2$ cluster size, and degree of disorder of carbon atoms can be obtained from the G peak position, half maximum of the G peak (G FWHM), and $I_D/I_G$ ratio of the peak area [55].

As shown in Fig. 4a, with an increase in the working pressure from 2 to 11 mTorr, both the G peak position and G FWHM remained stable around 1546 cm$^{-1}$ and 190 cm$^{-1}$, respectively, indicating a similar sp$^2$ hybridization percentage and structural disorder. The $I_D/I_G$ ratio, which corresponds to the sp$^2$ cluster size in the a-C films, exhibited irregular changes with the working pressure. From 2 to 5 mTorr, the $I_D/I_G$ ratio first decreased from its maximum value of 2.4 to 1.61, then increased to 1.98 when the working pressure was further increased to 11 mTorr, thus indicating the smallest size of the sp$^2$ cluster occurs at 5 mTorr.

Using XPS, the C and O elements were identified; the O element mainly came from residual oxygen in the chamber and pollutants in the air [56]. In Fig. S2b the Supporting Information, 20% Lorentzian and 80% Gaussian functions were used to fit the C 1s peak [57,58]. The content of sp$^2$ (284.6 eV), sp$^3$ (285.4 eV), and C–O/C=O (286.6 eV) hybrid carbon in the a-C films were calculated by fitting the peak areas, as shown in Fig. 4b, [59–61]. From 2 to 11 mTorr, all the three main species remained almost unchanged, and the sp$^2$ hybridization percentage reached around 55%. This high sp$^2$ content was favorable for achieving a better electron transfer capacity [62].

### *Electrochemical properties evaluation*

The electrochemical properties of the coated 316LSS were measured in a simulated PEMFC environment. As shown in Fig. 5a, the corrosion current densities of all the coated 316LSS

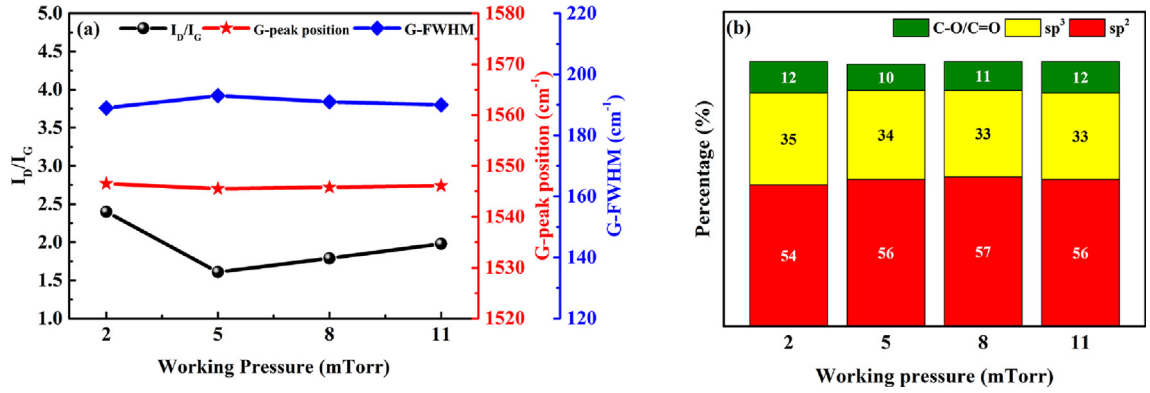


**Fig. 4 – (a) $I_D/I_G$ ratio, G peak position, and G FWHM; (b) sp$^2$, sp$^3$, and C–O/C=O hybrid carbon contents of a-C films deposited at 2–11 mTorr.**

samples were less than 1 μA/cm$^2$ (DOE 2025 standard) and much lower than that of the bare 316LSS sample [63]. In Fig. 5b, with the increase in working pressure from 2 to 11 mTorr, the corrosion current density showed an obvious increasing trend, from its minimum value of 0.27 μA/cm$^2$ at 2 mTorr to 0.68 μA/cm$^2$.

To assess the service life of the coated samples, potential holding tests were conducted for 12 h. In Fig. 5c, all the corrosion current densities decreased in the first 2 h and then stabilized. After the 12-h test, the final stable current densities increased with the increase in working pressure. The maximum value of the corrosion current density reached 0.006 μA/cm$^2$ at 11 mTorr, as shown in Fig. 5d, indicating the deterioration of the corrosion resistance of the a-C films with increasing working pressure.

Table 1 presents the concentrations of Fe and Cr ions in the corrosion solution after the long-term potentiostatic test. At 2 mTorr, no Cr or Fe signal could be detected, suggesting effective protection for 316LSS. At 5 and 8 mTorr, the Fe element could be detected, but its concentration was lower than that of bare 316LSS [63], indicating mild damage to 316LSS. At 11 mTorr, both the Cr and Fe ion concentrations suddenly increased, and the Fe ion concentration even exceeded 13 ppm, which was 20 times higher than that of bare 316LSS. This phenomenon may be due to the galvanic coupling between 316LSS and the a-C/Cr system in this corrosive solution, which can accelerate the corrosion of 316LSS [64].

### *ICR of the samples before and after potentiostatic polarization test*

Table 2 shows the ICR values before and after potentiostatic polarization tests under a compaction pressure of 1.5 MPa. For

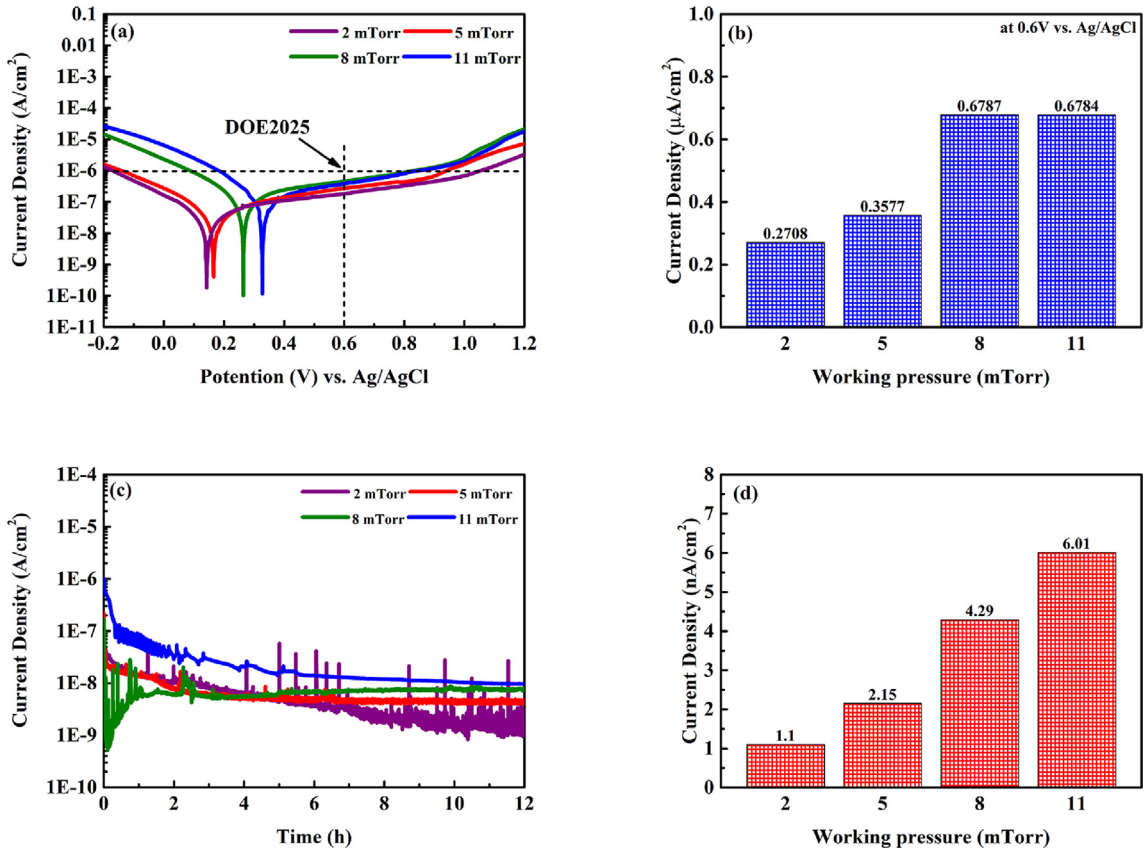


**Fig. 5 – Electrochemical polarization measurement in simulated cathode environment (a) potentiodynamic polarization curves, (b) passivated current densities; (c) potentiostatic tests curves, and (d) stable current densities after 12 h.**

**Table 1 – Concentrations of corrosion ions in the corrosion solution after 12 h of the potentiostatic test.**

| Sample | Concentrations of Cr ion (ppm) | Concentrations of Fe ion (ppm) |
|---|---|---|
| Substrate | 0.61 | 9.65 |
| a-C film (2 mTorr) | – | – |
| a-C film (5 mTorr) | – | 0.33 |
| a-C film (8 mTorr) | 0.03 | 0.57 |
| a-C film (11 mTorr) | 2.69 | 13.05 |

**Table 2 – The ICR values of the coated samples before and after the potentiostatic tests.**

| Sample | ICR (before tests) (mΩ·cm²) | | ICR (after tests) (mΩ·cm²) | |
|---|---|---|---|---|
| | 1.38 MPa | 1.5 MPa | 1.38 MPa | 1.5 MPa |
| a-C film (2 mTorr) | 2.2 | 2.0 | 2.9 | 2.7 |
| a-C film (5 mTorr) | 3.0 | 2.7 | 3.4 | 3.1 |
| a-C film (8 mTorr) | 3.3 | 3.0 | 3.7 | 3.4 |
| a-C film (11 mTorr) | 3.9 | 3.6 | 9.5 | 8.7 |

bare 316LSS, its ICR values before and after potentiostatic polarization tests are 12.10 and 19.28 mΩ · cm² [63], respectively.

All ICR values before and after the tests were lower than 10 mΩ · cm² (DOE 2025 standard), suggesting that the a-C films could significantly enhance the electrical conductivity. After the potentiostatic polarization test, the ICR of all the coated samples increased to a certain extent. At 1.38 MPa, from 2 to 8 mTorr, the ICR increase ratio was less than 32%; while, at 11 mTorr, the ICR increase ratio was larger than 144%, i.e., from 3.9 to 9.5 mΩ · cm², which was coincident with its worst anti-corrosion property.

### *Microstructural characterization after the potentiostatic tests*

The bonding structures in the a-C films before and after the potentiostatic tests were compared. In Fig. 6, both the $sp^2/sp^3$ ratio and C–O/C=O hybrid carbon content in the a-C film were nearly the same, suggesting no obvious damage and a stable surface chemical composition of the a-C films during the test.

The microstructural evolution inside the a-C films was also investigated. In Fig. 7a and c, three interesting areas of the a-C film prepared at 5 mTorr are marked, namely, the near surface (labeled as $a_1$ and $a_2$), middle part (labeled as $b_1$ and $b_2$), and near interface area (labeled as $c_1$ and $c_2$). EELS is the preferred method for the quantitative extraction of $sp^2$ from carbon-based materials at high spatial resolution [65]. The carbon-based part of the spectrum was decomposed into π* and σ* characteristics by the "Two-window method" [66]. In Fig. 7b and d, the π* peak center at 285 eV was fitted by the Gaussian function, and the integration of the peak σ* in the small energy window of 290–305 eV was performed. The content of $sp^2$ (x) is calculated using the following equation [66,67]:

$$\frac{(\pi^*/\sigma^*)_{film}}{(\pi^*/\sigma^*)_{std}} = \frac{3x}{4-x} \quad (3)$$

where $(\pi^*/\sigma^*)_{film}$ and $(\pi^*/\sigma^*)_{std}$ represent the integral area ratio of the π* and σ* peaks for the a-C film and the reference sample, respectively. Highly oriented pyrolytic graphite (HOPG) was selected as the standard sample for the analysis of carbon bonds. The calculated $sp^2/sp^3$ values at areas $b_1/b_2$ and $c_1/c_2$ of the a-C film were all approximately 1.13, which is consistent with the previous XPS analysis. However, the $sp^2/sp^3$ values at the position $a_1/a_2$ near the a-C film surface were all approximately 1.35, which was slightly higher than the $sp^2/sp^3$ values at other positions. The EELS curves in the same areas were nearly unchanged after the polarization test, confirming that the composition of the a-C film remained stable.

Both the XPS and EELS results showed that the long-term potentiostatic test had little effect on the structure of the a-C films.

### *Relationship between working pressure and performance degradation*

To reveal the relationship between the working pressure and the performance of a-C films in PEMFCs, the plasma states during deposition, compactness, and composition of the as-deposited a-C films should be discussed.

From the microstructural characterization of the a-C film, before and after the long-term electrochemical corrosion, a stable structure of a-C films and interface damage can be confirmed. However, the damage of the interface was affected by the compactness and composition of the a-C film, which can be greatly influenced by the plasma state. First, the structure and growth process of the a-C films can be affected by the energy of incident particles on the substrates during deposition [68,69]. According to the plasma diagnosis results, when the pressure increased 4 times; that is, from 2 to 8 mTorr, although both the electron density and plasma potential in the cavity increased, the actual ionization degree of the DCMS plasma decreased sharply. Finally, less energetic ions in the plasma resulted in an incompact structure and a lower density of the a-C films.

For these hydrogen-free a-C films, their density is mainly related to the $sp^2/sp^3$ ratio and the presence of microvoids and defects [49,70]. As confirmed by Raman, XPS, and EELS

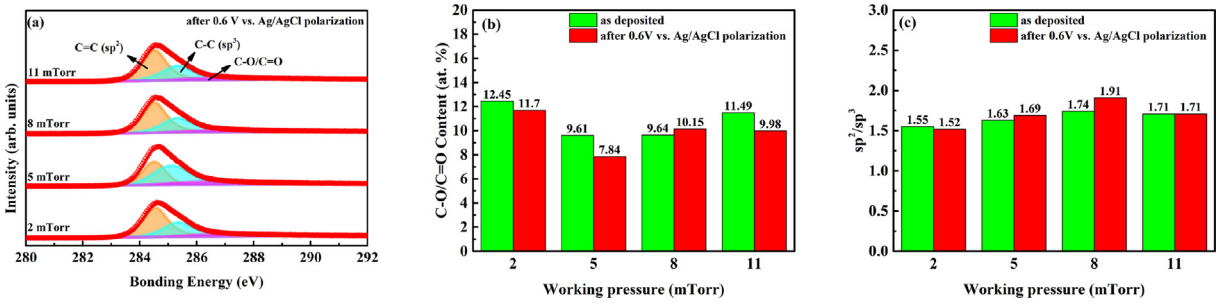


**Fig. 6 – Composition of a-C films after potentiostatic test (a) The C1s core-level spectra, (b) $sp^2/sp^3$ and C–O/C=O hybrid carbon content.**

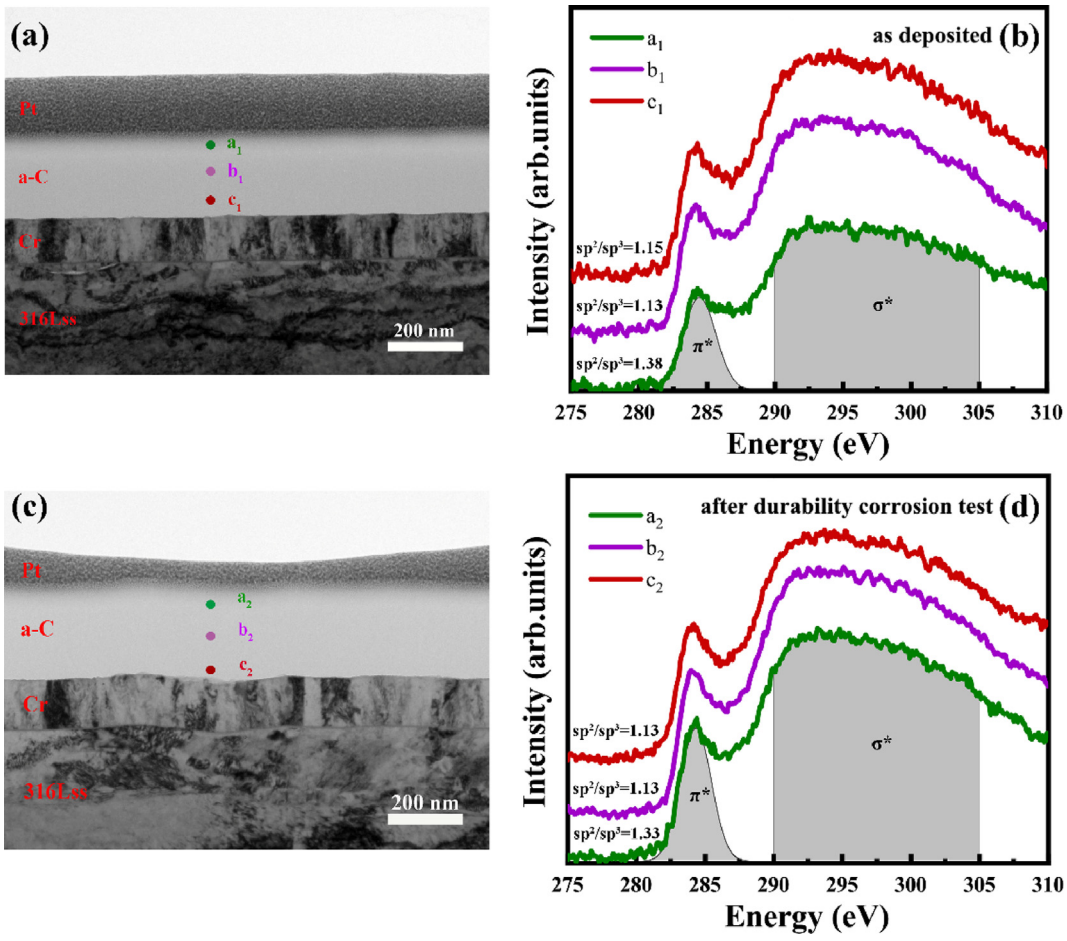


**Fig. 7 – The STEM image of the a-C film deposited at 5 mTorr and EELS spectra at different areas marked as $a_1$-$c_1$ and $a_2$-$c_2$ (a, b) before and (c, d) after the long-time potentiostatic test.**

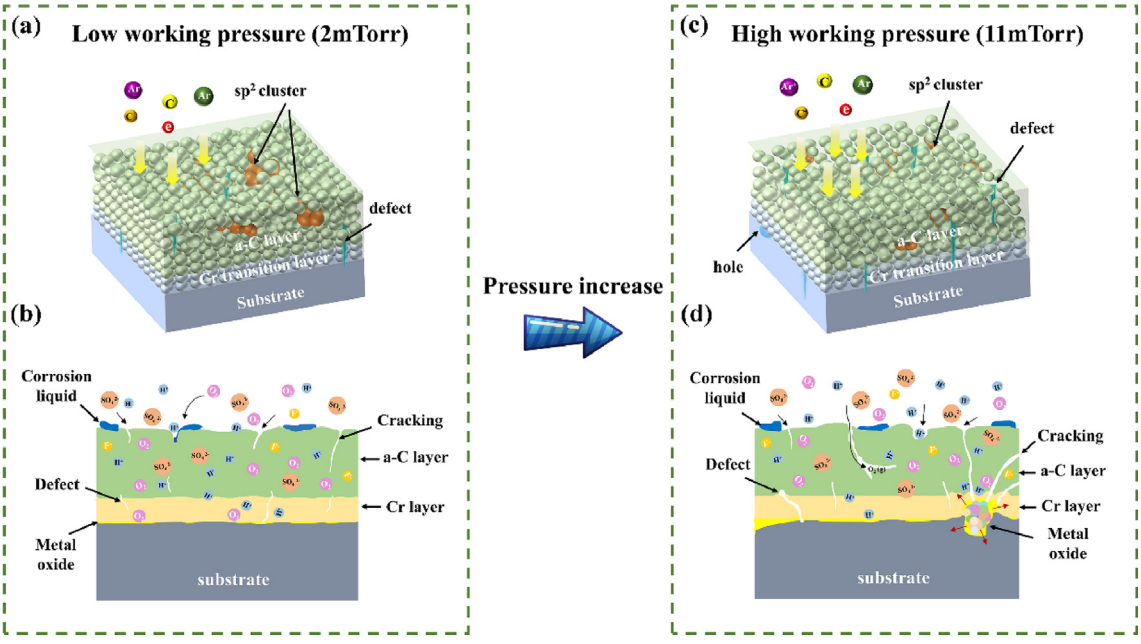


**Fig. 8 – The degradation mechanism of a-C film deposited at low and high working pressure; (b) Interfacial corrosion process with dense structures; (c) a-C film structure with high working pressure; (d) Interfacial corrosion process with loose structures.**

analyses, in the working pressure range of 2–11 mTorr, the $sp^2$ content of the a-C films remained stable. In this case, their density measured by XRR can roughly corresponds to the number of microvoids or defects in the a-C films; that is, the higher density of the a-C films indicated fewer defects and a compact structure.

In the corrosion and ICR tests, the a-C film prepared at 2 mTorr exhibited the best corrosion resistance and conductivity. Two main factors should be considered: First, this sample had the highest density approximately 2.52 g/cm$^3$ and a compact structure, which can hinder the corrosion liquid entering the a-C film and cause less oxide to form at the interface. In addition, the sample had the maximum $I_D/I_G$ ratio of 2.4 and the largest $sp^2$ cluster size, which is conducive to electron transport, resulting in the minimum ICR before corrosion tests, as shown in Fig. 8(a–b). Because of its superior corrosion resistance, no Fe and Cr signals could be detected in the corrosion solution, and the ICR after 12 h of polarization test was still the lowest.

At 11 mTorr, the density and compactness of the a-C films decreased, while its $sp^2$ cluster size was still large, which can lead to better conductivity. During the corrosion test, the corrosion solution can reach the 316LSS substrate faster and easily move along the loose structure and defect of the a-C film. The possible galvanic coupling between 316LSS and the a-C/Cr system can cause serious damage and more oxides at the interface, resulting in worse corrosion resistance, more Fe and Cr concentration in the corrosive solution, and higher ICR, as shown in Fig. 8(c–d).

## Conclusions

In this study, a series of a-C/Cr/316LSS samples were prepared using DCMS. The effects of compactness and composition on the performance of the a-C films in PEMFCs were investigated. The results showed that, with an increase in the working pressure from 2 to 11 mTorr, the ionization degree of the plasma decreased sharply, which caused a decrease in the compactness of the a-C films. The a-C film deposited at 2 mTorr had both the highest compactness (2.52 g/cm$^3$) and large $sp^2$ cluster size, demonstrating the best corrosion resistance and conductivity. For the a-C film with low density and small $sp^2$ cluster size, performance degradation and interface damage were observed; at 11 mTorr, the a-C film had both a loose structure and large $sp^2$ cluster size. The possible galvanic coupling between 316LSS and the a-C/Cr system can result in serious performance degradation. These results reveal that high-density plasma is pivotal to obtain a compact microstructure of the a-C film; both high compactness and $sp^2$ clusters of the a-C should be simultaneously considered for the protection of metallic BPPs in PEMFCs.

## Declaration of competing interest

The authors declare that they have no known competing financial interests or personal relationships that could have appeared to influence the work reported in this paper.

## Acknowledgment

This work was financial supported by National Natural Science Foundation of China (52025014), Zhejiang Lingyan Research and Development Program (2022C01113), K.C.Wong Education Foundation (GJTD-2019-13), CAS Interdisciplinary Innovation Team (292020000008), CAS-NST Joint Research Project (174433KYSB20200021) and Natural Science Foundation of Ningbo (202003N4350). We appreciate Dr Xiao Zuo at Huawei Technologys Co., Ltd. on plasma analyze and discussion. We also thank the assistance of Dr Xiaolong Zhou at Shenzhen Institutes of Advanced Technology, Chinese Academy of Sciences, and Dr Yanxin Dan at Nagaoka University of Technology for XRR measurement and discussion.

## Appendix A. Supplementary data

Supplementary data to this article can be found online at https://doi.org/10.1016/j.ijhydene.2022.01.173.

## REFERENCES

[1] Tu Z, Zhang H, Luo Z, Liu J, Wan Z, Pan M. Evaluation of 5kW proton exchange membrane fuel cell stack operated at 95°C under ambient pressure. J Power Sources 2013;222:277–81.
[2] Fukutsuka T, Yamaguchi T, Miyano S-I, Matsuo Y, Sugie Y, Ogumi Z. Carbon-coated stainless steel as PEFC bipolar plate material. J Power Sources 2007;174:199–205.
[3] Song Y, Zhang C, Ling C-Y, Han M, Yong R-Y, Sun D, et al. Review on current research of materials, fabrication and application for bipolar plate in proton exchange membrane fuel cell. Int J Hydrogen Energy 2020;45:29832–47.
[4] Heinzel A, Mahlendorf F, Niemzig O, Kreuz C. Injection moulded low cost bipolar plates for PEM fuel cells. J Power Sources 2004;131:35–40.
[5] Wang H-C, Hou K-H, Lu C-E, Ger M-D. The study of electroplating trivalent CrC alloy coatings with different current densities on stainless steel 304 as bipolar plate of proton exchange membrane fuel cells. Thin Solid Films 2014;570:209–14.
[6] Feng K, Li Z, Cai X, Chu PK. Silver implanted 316L stainless steel as bipolar plates in polymer electrolyte membrane fuel cells. Mater Chem Phys 2011;126:6–11.
[7] Feng K, Shen Y, Mai J, Liu D, Cai X. An investigation into nickel implanted 316L stainless steel as a bipolar plate for PEM fuel cell. J Power Sources 2008;182:145–52.
[8] Wang S-H, Peng J, Lui W-B, Zhang J-S. Performance of the gold-plated titanium bipolar plates for the light weight PEM fuel cells. J Power Sources 2006;162:486–91.
[9] Bi FF, Yi PY, Zhou T, Peng LF, Lai XM. Effects of Al incorporation on the interfacial conductivity and corrosion resistance of CrN film on SS316L as bipolar plates for proton exchange membrane fuel cells. Int J Hydrogen Energy 2015;40:9790–802.
[10] Wan Z, Zhang TF, Lee HB, Yang JH, Choi WC, Han B, et al. Improved corrosion resistance and mechanical properties of CrN hard coatings with an atomic layer deposited Al2O3 interlayer. ACS Appl Mater Interfaces 2015;7:26716–25.
[11] Zhang M, Wu B, Lin GQ, Shao ZG, Hou M, Yi BL. Arc ion plated Cr/CrN/Cr multilayers on 316L stainless steel as bipolar

plates for polymer electrolyte membrane fuel cells. J Power Sources 2011;196:3249–54.
[12] Wang Y, Northwood DO. An investigation of the electrochemical properties of PVD TiN-coated SS410 in simulated PEM fuel cell environments. Int J Hydrogen Energy 2007;32:895–902.
[13] Mohammadi N, Yari M, Allahkaram SR. Characterization of PbO2 coating electrodeposited onto stainless steel 316L substrate for using as PEMFC's bipolar plates. Surf Coating Technol 2013;236:341–6.
[14] Hansen MK, Aili D, Christensen E, Pan C, Eriksen S, Jensen JO, et al. PEM steam electrolysis at 130 °C using a phosphoric acid doped short side chain PFSA membrane. Int J Hydrogen Energy 2012;37:10992–1000.
[15] Negi S, Bhandari R, Rieth L, Solzbacher F. In vitro comparison of sputtered iridium oxide and platinum-coated neural implantable microelectrode arrays. Biomed Mater 2010;5:15007.
[16] Bi F, Li X, Yi P, Hou K, Peng L, Lai X. Characteristics of amorphous carbon films to resist high potential impact in PEMFCs bipolar plates for automotive application. Int J Hydrogen Energy 2017;42:14279–89.
[17] Yi P, Peng L, Feng L, Gan P, Lai X. Performance of a proton exchange membrane fuel cell stack using conductive amorphous carbon-coated 304 stainless steel bipolar plates. J Power Sources 2010;195:7061–6.
[18] Wang J, Sun J, Li S, Wen Z, Ji S. Surface diffusion modification AISI 304SS stainless steel as bipolar plate material for proton exchange membrane fuel cell. Int J Hydrogen Energy 2012;37:1140–4.
[19] Mawdsley JR, Carter JD, Wang XP, Niyogi S, Fan CQ, Koc R, et al. Composite-coated aluminum bipolar plates for PEM fuel cells. J Power Sources 2013;231:106–12.
[20] Mendizabal L, Oedegaard A, Kongstein OE, Leedre S, Walmsley J, Barriga J, et al. TaNx coatings deposited by HPPMS on SS316L bipolar plates for polymer electrolyte membrane fuel cells: correlation between corrosion current, contact resistance and barrier oxide film formation. Int J Hydrogen Energy 2017;42:3259–70.
[21] Yi P, Zhang D, Qiu D, Peng L, Lai X. Carbon-based coatings for metallic bipolar plates used in proton exchange membrane fuel cells. Int J Hydrogen Energy 2019;44:6813–43.
[22] Lu C-E, Pu N-W, Hou K-H, Tseng C-C, Ger M-D. The effect of formic acid concentration on the conductivity and corrosion resistance of chromium carbide coatings electroplated with trivalent chromium. Appl Surf Sci 2013;282:544–51.
[23] Wu Mingge LC, Hong Tao, Chen Guohai, Wen Donghui, Zhang Haifeng, Zhang Dong. Chromium interlayer amorphous carbon film for 304 stainless steel bipolar plate of proton exchange membrane fuel cell. Surf Coating Technol 2016;307:374–81.
[24] Wu B, Lin G, Fu Y, Hou M, Yi B. Chromium-containing carbon film on stainless steel as bipolar plates for proton exchange membrane fuel cells. Int J Hydrogen Energy 2010;35:13255–61.
[25] Bi F, Hou K, Yi P, Peng L, Lai X. Mechanisms of growth, properties and degradation of amorphous carbon films by closed field unbalanced magnetron sputtering on stainless steel bipolar plates for PEMFCs. Appl Surf Sci 2017;422:921–31.
[26] Yi P, Zhang W, Bi F, Peng L, Lai X. Microstructure and properties of a-C films deposited under different argon flow rate on stainless steel bipolar plates for proton exchange membrane fuel cells. J Power Sources 2019;410–411:188–95.
[27] Li H, Guo P, Zhang D, Liu LL, Wang ZY, Ma GS, et al. Interface-induced degradation of amorphous carbon films/stainless steel bipolar plates in proton exchange membrane fuel cells. J Power Sources 2020;469:228269.
[28] Mingge W, Congda L, Tao H, Guohai C, Donghui W, Haifeng Z, et al. Chromium interlayer amorphous carbon film for 304 stainless steel bipolar plate of proton exchange membrane fuel cell. Surf Coating Technol 2016;307:374–81.
[29] Mingge W, Congda L, Dapeng T, Tao H, Guohai C, Donghui W. Effects of metal buffer layer for amorphous carbon film of 304 stainless steel bipolar plate. Thin Solid Films 2016;616:507–14.
[30] Hirata Y, Kitamura K, Ishikawa T, Choi J. Effect of precursor gas on the structure and mechanical properties of hydrogenated amorphous carbon films deposited on a trench sidewall. J Appl Phys 2019;125:065306.
[31] Wang C, Jiang F, Wang F. Cerium chemical conversion coating for aluminum alloy 2024-T3 and its corrosion resistance. Corrosion 2004;60:237–43.
[32] Wang ZY, Feng K, Li ZG, Lu FG, Huang J, Wu YX, et al. Self-passivating carbon film as bipolar plate protective coating in polymer electrolyte membrane fuel cell. Int J Hydrogen Energy 2016;41:5783–92.
[33] Marcinkoski J, Kopasz JP, Benjamin TG. Progress in the US DOE fuel cell subprogram efforts in polymer electrolyte fuel cells. Int J Hydrogen Energy 2008;33:3894–902.
[34] Zuo X, Zhang D, Chen R, Ke P, Odén M, Wang A. Spectroscopic investigation on the near-substrate plasma characteristics of chromium HiPIMS in low density discharge mode. Plasma Sources Sci Technol 2020;29:015013.
[35] Li H, Guo P, Zhang D, Chen R, Zuo X, Ke P, et al. Influence of deposition temperature on the structure, optical and electrical properties of a-C films by DCMS. Appl Surf Sci 2020;503:144310.
[36] Deringer VL, Caro MA, Jana R, Aarva A, Elliott SR, Laurila T, et al. Computational surface chemistry of tetrahedral amorphous carbon by combining machine learning and density functional theory. Chem Mater 2018;30:7438–45.
[37] Parratt LG. Surface studies of solids by total reflection of X-rays. Phys Rev 1954;95:359–69.
[38] Gago Mv R, Jäger HU, Belov A Yu, Jiménez I. Evolution of $sp^2$ networks with substrate temperature in amorphous carbon films: experiment and theory. Phys Rev B 2005;72:014120.
[39] Zhang D, Yi P, Peng L, Lai X, Pu J. Amorphous carbon films doped with silver and chromium to achieve ultra-low interfacial electrical resistance and long-term durability in the application of proton exchange membrane fuel cells. Carbon 2019;145:333–44.
[40] Wang Y, Northwood DO. Effects of $O^2$ and $H^2$ on the corrosion of SS316L metallic bipolar plate materials in simulated anode and cathode environments of PEM fuel cells. Electrochim Acta 2007;52:6793–8.
[41] Carvalho I, Dias N, Henriques M, Calderon VS, Ferreira P, Cavaleiro A, et al. Antibacterial effects of bimetallic clusters incorporated in amorphous carbon for stent application. ACS Appl Mater Interfaces 2020;12:24555–63.
[42] Högström J, Andersson M, Jansson U, Björefors F, Nyholm L. On the evaluation of corrosion resistances of amorphous chromium-carbon thin-films. Electrochim Acta 2014;122:224–33.
[43] Papadias DD, Ahluwalia RK, Thomson JK, Meyer HM, Brady MP, Wang H, et al. Degradation of SS316L bipolar plates in simulated fuel cell environment: corrosion rate, barrier film formation kinetics and contact resistance. J Power Sources 2015;273:1237–49.
[44] Fu Y, Hou M, liang D, Yan X, Fu Y, Shao Z, et al. The electrical resistance of flexible graphite as flowfield plate in proton exchange membrane fuel cells. Carbon 2008;46:19–23.
[45] Maheshwari P, Bhattacharya D, Sharma SK, Mukherjee S, Samanta S, Basu S, et al. Probing inhomogeneities in nanoscale organic semiconductor films: depth profiling using slow positron beam and X-ray reflectivity techniques. Solid State Commun 2014;200:22–8.
[46] Konkhunthot N, Tunmee S, Zhou X, Komatsu K, Photongkam P, Saitoh H, et al. The correlation between

optical and mechanical properties of amorphous diamond-like carbon films prepared by pulsed filtered cathodic vacuum arc deposition. Thin Solid Films 2018;653:317–25.
[47] Zhou X, Tunmee S, Suzuki T, Phothongkam P, Kanda K, Komatsu K, et al. Quantitative NEXAFS and solid-state NMR studies of $sp^3/(sp^2 + sp^3)$ ratio in the hydrogenated DLC films. Diam Relat Mater 2017;73:232–40.
[48] Persson D, Thierry D, LeBozec N, Prosek T. In situ infrared reflection spectroscopy studies of the initial atmospheric corrosion of Zn–Al–Mg coated steel. Corrosion Sci 2013;72:54–63.
[49] Liu L, Wang T, Huang J, He Z, Yi Y, Du K. Diamond-like carbon thin films with high density and low internal stress deposited by coupling DC/RF magnetron sputtering. Diam Relat Mater 2016;70:151–8.
[50] Li HX, Xu T, Chen JM, Zhou HD, Liu HW. The effect of applied dc bias voltage on the properties of a-C:H films prepared in a dual dc–rf plasma system. Appl Surf Sci 2004;227:364–72.
[51] Mohagheghpour E, Rajabi M, Gholamipour R, Larijani MM, Sheibani S. Correlation study of structural, optical and electrical properties of amorphous carbon thin films prepared by ion beam sputtering deposition technique. Appl Surf Sci 2016;360:52–8.
[52] Folkenant M, Nygren K, Malinovskis P, Palisaitis J, Persson POÅ, Lewin E, et al. Structure and properties of Cr–C/Ag films deposited by magnetron sputtering. Surf Coating Technol 2015;281:184–92.
[53] Xing T, Li LH, Hou L, Hu X, Zhou S, Peter R, et al. Disorder in ball-milled graphite revealed by Raman spectroscopy. Carbon 2013;57:515–9.
[54] Ribeiro-Soares J, Oliveros ME, Garin C, David MV, Martins LGP, Almeida CA, et al. Structural analysis of polycrystalline graphene systems by Raman spectroscopy. Carbon 2015;95:646–52.
[55] Chu PK, Li L. Characterization of amorphous and nanocrystalline carbon films. Mater Chem Phys 2006;96:253–77.
[56] Nakao S, Yukimura K, Nakano S, Ogiso H. DLC coating by HiPIMS: the Iinfluence of substrate bias voltage. IEEE Trans Plasma Sci 2013;41:1819–29.
[57] Yusuke Taki OT. XPS structural characterization of hydrogenated amorphous carbon thin films prepared by shielded arc ion plating. Thin Solid Films 1998;316:45–50.
[58] Filik J, May PW, Pearce SRJ, Wild RK, Hallam KR. XPS and laser Raman analysis of hydrogenated amorphous carbon films. Diam Relat Mater 2003;12:974–8.
[59] Guo P, Li X, Sun L, Chen R, Ke P, Wang A. Stress reduction mechanism of diamond-like carbon films incorporated with different Cu contents. Thin Solid Films 2017;640:45–51.
[60] Pandiyan R, Delegan N, Dirany A, Drogui P, El Khakani MA. Correlation of $sp^2$ carbon bonds content in magnetron-sputtered amorphous carbon films to their electrochemical $H_2O_2$ production for water decontamination applications. Carbon 2015;94:988–95.
[61] Dwivedi N, Yeo RJ, Satyanarayana N, Kundu S, Tripathy S, Bhatia CS. Understanding the role of nitrogen in plasma-assisted surface modification of magnetic recording media with and without ultrathin carbon overcoats. Sci Rep 2015;5:7772.
[62] Li X, Peng L, Zhang D, Yi P, Lai X. The frequency of pulsed DC sputtering power introducing the graphitization and the durability improvement of amorphous carbon films for metallic bipolar plates in proton exchange membrane fuel cells. J Power Sources 2020;466:228346.
[63] Li H, Guo P, Zhang D, Liu L, Wang Z, Ma G, et al. Interface-induced degradation of amorphous carbon films/stainless steel bipolar plates in proton exchange membrane fuel cells. J Power Sources 2020;469:228269.
[64] Qiu J, Wu A, Li Y, Xu Y, Scarlat R, Macdonald DD. Galvanic corrosion of Type 316L stainless steel and Graphite in molten fluoride salt. Corrosion Sci 2020;170:108677.
[65] Bernier N, Bocquet F, Allouche A, Saikaly W, Brosset C, Thibault J, et al. A methodology to optimize the quantification of $sp^2$ carbon fraction from K edge EELS spectra. J Electron Spectrosc Relat Phenom 2008;164:34–43.
[66] Galvan D, Pei YT, De Hosson JTM, Cavaleiro A. Determination of the $sp^3$ C content of a-C films through EELS analysis in the TEM. Surf Coating Technol 2005;200:739–43.
[67] Xie J, Komvopoulos K. The effect of Argon ion irradiation on the thickness and structure of ultrathin amorphous carbon films. J Appl Phys 2016;119:095304.
[68] Cai JB, Wang XL, Bai WQ, Zhao XY, Wang TQ, Tu JP. Bias-graded deposition and tribological properties of Ti-contained a-C gradient composite film on Ti6Al4V alloy. Appl Surf Sci 2013;279:450–7.
[69] Barnat EV, Lu TM. Calculated sheath dynamics under the influence of an asymmetrically pulsed dc bias. Phys Rev E - Stat Nonlinear Soft Matter Phys 2002;66:056401.
[70] Toney MF, Brennan S. Measurements of carbon thin films using x-ray reflectivity. J Appl Phys 1989;66:1861–3.